Volume 27
Number 34
14 September 2025
Pages 17617–18040

PCCP

Physical Chemistry Chemical Physics

rsc.li/pccp

25 YEARS ANNIVERSARY

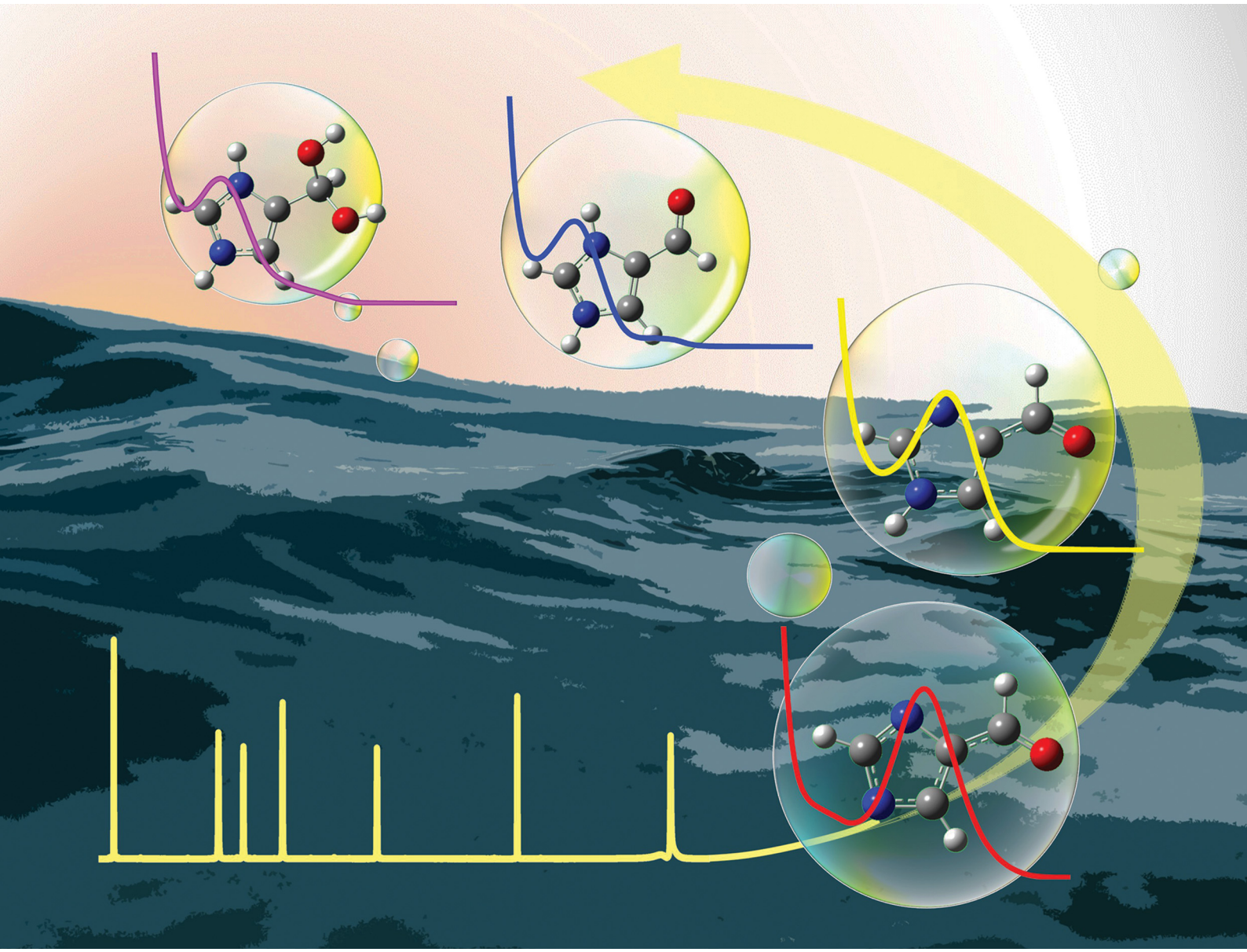

ISSN 1463-9076

ROYAL SOCIETY OF CHEMISTRY

PAPER

Juan G. Navea *et al.*

pH-Dependent absorption spectra of aqueous 4-imidazolecarboxaldehyde: theoretical and experimental insights into a marine chromophore proxy

PCCP Owner Societies

PCCP

PAPER

View Article Online
View Journal | View Issue

Cite this: *Phys. Chem. Chem. Phys.*, 2025, **27**, 17673

pH-Dependent absorption spectra of aqueous 4-imidazolecarboxaldehyde: theoretical and experimental insights into a marine chromophore proxy

Lily J. Watson, Elizabeth Scholer, Caroline H. V. Calvert and Juan G. Navea *

The sea surface microlayer (SSML) contains light-absorbing organic chromophores known to initiate daytime aqueous-phase chemistry in the environment. These compounds, referred to as marine chromophoric dissolved organic matter (m-CDOM), are known to partition from the sea surface into sea spray aerosol (SSA), where they undergo substantial changes in acidity, transitioning from the slightly basic SSML to the more acidic SSA. Recent studies suggest that the photosensitizing efficiency of m-CDOM is pH-dependent, but its chemical complexity hinders direct molecular-level investigation. Because m-CDOM contains more nitrogen than its terrestrial counterpart, 4-imidazolecarboxaldehyde (4IC)—a nitrogen-containing chromophore and known photosensitizer—has served as an effective model system form m-CDOM. Yet, little is known about its pK_a values or how its optical properties respond to the variable pH conditions characteristic of the marine atmosphere. Understanding the pH-dependent behavior of 4IC is essential for modeling the photochemical behavior of nitrogen-rich marine chromophores. Here, we characterize the speciation and optical properties of 4IC across a wide pH range, reporting its pK_a and the pH effect in its absorption features. The diol-aldehyde equilibrium of 4IC, along with the optical properties of the species involved, was also investigated in the context of daytime chemistry in the marine environment. Using theoretical and experimental techniques, we show that the protonation state of 4IC significantly affects its electronic transitions. Under acidic conditions typical of submicron SSA, 4IC exhibits low-energy absorption bands that overlap with the solar spectrum, with more intense high-energy features extending into the actinic region. As pH increases to values characteristic of the SSML, the more intense band redshifts towards the solar spectrum. Theoretical results closely match experimental trends, reproducing the redshift and accurately predicting the energies of key transitions.

Received 23rd April 2025,
Accepted 26th July 2025

DOI: 10.1039/d5cp01553g

rsc.li/pccp

Introduction

Environmental organic chromophores play a pivotal role in daytime chemistry, influencing gas evolution, new particle formation, redox cycling, and the marine chemical balance.[1–9] In the marine boundary layer (MBL), these organic chromophores are a significant component of marine dissolved organic matter (m-DOM), which is among the most prevalent light-absorbing substances in the marine environment.[9–12] The light-absorbing fraction of m-DOM, known as marine chromophoric dissolved organic matter (m-CDOM), has absorbance features that overlap with the solar spectrum, making it an effective photosensitizer and initiating photochemistry in the sea surface microlayer (SSML).[13–19] Once partitioned into sea spray aerosols, m-CDOM facilitates photochemical reactions that influence atmospheric composition, aerosol properties, and the chemical balance in the marine atmosphere.[20–23] Understanding the properties of m-CDOM is essential for advancing our molecular-level knowledge of chemistry and photochemistry in the MBL. Particularly, the synergy between experimental methods and theoretical modeling has offered valuable insights into the mechanisms of molecular photoactivation in aqueous environments and at complex environmental interfaces.[24–27]

Marine dissolved organic matter (m-DOM) is present in low concentrations and is unpredictably distributed throughout the ocean, making its extraction challenging.[13] Due to their similarity in optical properties with m-DOM, humic substances (HS) are sometimes used as proxies, though their chemical complexity makes characterization equally difficult to study.[13,28–33] Thus, molecular model compounds—such as benzoic acid, gallic

Chemistry Department, Skidmore College, Saratoga Springs, NY 12866-1632, USA. E-mail: jnavea@skidmore.edu

acid, and 4-benzoylbenzoic acid (4BBA)—have been used to probe specific chemical and physical processes relevant to environmental photochemistry.[25,26,34] However, during the 2019 SeaSCAPE mesocosm campaign, a general compositional analysis of m-CDOM was achieved, revealing that, while it shares chemical features with terrestrial HS—including aromatic ketones, carboxylated alicyclic molecules, and aromatic carboxylic acids—m-CDOM is characterized by a higher presence of nitrogen-rich chromophores compared to its terrestrial counterpart.[16] This characteristic has been shown to influence various environmental processes, such as the water uptake ability of organic aerosols and the photosensitization that occurs at environmental interfaces.[17,19,35] However, the traditional model compounds mentioned above lack nitrogen heteroatoms and therefore do not capture these nitrogen-dependent chromophoric features of marine-derived DOM.

The identification of nitrogen-rich chromophores in m-CDOM has thus highlighted the need for new molecular models that incorporate this functionality, enabling a better representation of photochemistry in the MBL.[36] In this context, recent studies have identified imidazole-carboxaldehyde compounds, such as 4-imidazolecarboxaldehyde (4IC) and its isomers, in atmospheric particles.[37–39] These compounds are increasingly recognized as valuable molecular models for nitrogen-containing chromophores within atmospheric particles, including marine photosensitizers.[17,40] Among these, 4IC stands out for its small size, structural simplicity, and availability, making it especially well-suited for molecular-level analysis. Its prior use in marine aerosol studies further supports its potential as a representative and tractable proxy for nitrogen-containing chromophores.[17] However, the use of 4IC as a proxy for m-CDOM and other environmental chromophores is constrained by the lack of detailed spectroscopic and acid–base characterization under environmentally relevant conditions.

Environmental conditions, such as pH, can add complexity to the already intricate chemical composition of environmental chromophores, shifting their acid–base equilibrium and changing their speciation.[24–27] While m-CDOM in the surface layers of natural waters, including the SSML, typically exists at a slightly basic pH, it can transition to an acidic medium with pH levels as low as 2 when it partitions into spray aerosols.[41,42] This variation in pH can lead to significant changes in the absorption spectra of environmental photosensitizers, with the concomitant impact in the rate and yield of photochemical reactions across the ocean–air interface.[3,13] In particular, the photoactivity of 4IC, like those of other chromophores within m-CDOM, can change with pH. Thus, to better understand the photochemistry of 4IC, it is paramount to investigate the pH-induced changes in its optical properties. Although the 4IC molecule is a relatively simple system, the absorbance spectra change due to the protonation and deprotonation of nitrogen atoms, as well as hydration of the aldehyde group to form a geminal diol, has not been investigated.

The use of models, such as 4IC, for molecular-level studies of environmental photosensitizers requires a careful examination of their physical and chemical properties under conditions relevant to the environment. This work integrates experimental spectroscopic studies with theoretical calculations to explore the absorbance spectra of 4IC in aqueous solutions across different pH levels in relation to the solar spectral flux. This approach offers insights into the contributions of different speciated forms of 4IC in its optical absorption spectrum. Our theoretical studies allow the visualization of the nature of the excited states of 4IC, as well as an understanding of the effects of solvating water molecules, the orbitals involved in electron transitions, and how the contributions of speciated forms shape the 4IC optical spectrum at different pH levels.

Experimental section

Optical properties and speciation analysis

Sample 4-imidazolecarboxaldehyde (4IC), purchased from Sigma Aldrich and used without further purification, was dissolved in 18 MΩ Milli-Q water to prepare 100 mM aqueous solutions. The pH was adjusted by adding known volumes of either hydrochloric acid (1 N) or sodium hydroxide (1 N), both obtained from Fisher Chemical. UV-vis spectra of a 100 mM 4IC solution were acquired at pH values ranging from 1.0 to 13.0, with all pH measurements performed using an ACCUMET AB15 pH meter. Ionic strength across the pH range remained low, with a maximum of approximately 0.1 M near pH 13. While slight uncertainty is expected at high pH due to alkaline error, measurements remained within the meter's calibrated range and were consistent with pH indicator paper. Thus, pH 13 is used as a reasonable approximation of strongly basic conditions. Spectral data were collected on a PerkinElmer Lambda 35 spectrophotometer using 1 cm quartz cuvettes.

The pK_a values were determined using potentiometric titration and ^{1}H-NMR titration. ^{1}H-NMR spectroscopy of 4IC solutions was performed using a Jeol 400 MHz instrument with solvent suppression in the acquisition parameters. All ^{1}H-NMR were collected for 4IC solutions with pH ranging from 1.0 to 13.0. The NMR samples contained 5 mM of sodium trimethylsilylpropanesulfonate (DSS), purchased from Sigma Aldrich, as internal standard for peak locking. To provide additional pK_a analyses, potentiometric titrations were conducted on acidified 100 mM 4IC solutions by adding, dropwise, 0.3 M solution of NaOH. Titrant addition followed a 15-minute N_2 bubbling period, with all subsequent measurements conducted under a continuous flow of 15 standard cubic feet per hour (scfh) to remove CO_2 and other trace gases, minimizing pH fluctuations caused by H_2CO_3 formation.

All measurements, including UV-vis, ^{1}H-NMR, and potentiometric titrations, were conducted at a constant temperature of 22 °C.

Theoretical models and methods

Water solvation plays a crucial role in the electronic excitation of chromophores, significantly impacting the accuracy of simulated spectra. Recent works shows that that without explicitly

including water molecules in the model, it is nearly impossible to reproduce experimental spectra, particularly at low and high pH conditions where charged protonated and deprotonated species prevail.[24–26,34] In particular, recent research has shown that incorporating eight water molecules provides the best agreement with experiment, accurately capturing band intensity, shape, and energy.[25,34] Therefore, clusters of 4IC species with 8 water molecules were considered – 4IC·$(H_2O)_8$. The initial water cluster structure and its position near 4IC were modeled based on the methods implemented in the theoretical study of benzoic acid and 4-benzoyl benzoic acid.[26,34] GaussView program was used to randomly distribute eight water molecules around the 4IC molecule, with 4IC positioned at the center of a cluster sphere. Additional local minima were generated by reallocating water molecules, near the carbonyl, diols, amine, and imine functional groups of each 4IC form modeled (Fig. S1) to capture a range of potential hydrogen bonding interactions.

All theoretical calculations for small clusters 4IC·$(H_2O)_8$ were conducted using the quantum chemical computational software Gaussian 09 and visualized using GaussView. Geometry optimizations, excited states, and energy calculations were carried out using density functional theory (DFT) and time-dependent DFT (TD-DFT) level of theory, with Becke's three-parameter hybrid method with the LYP correlation functional (B3LYP) and basis set 6-311++G(d,p).[43] Additionally, all cluster calculations used dispersion corrections from Grimme's DFT-D2 method.[44] For each excitation energy, the vertical transitions were convoluted using Chemissian software package, which first convolutes the spectrum with a chosen Gaussian width in energy units (eV) before being converted to wavelength (nm). Each vertical transition was convoluted with a Gaussian line shape (half-width = 0.330 eV), and the resulting functions were summed to generate the excitation spectrum. To describe the nature of the excited states, the hole/particle natural transition orbitals (NTOs)[45,46] pairs were calculated for every excited state involved in the formation of each absorption band.

To better understand the water–4IC interaction as a function of pH, theoretical spectra of all experimentally determined forms of 4IC, as described in Scheme 1, were simulated and compared with UV-vis spectral data of 4IC at the appropriate pH. Based on the pK_a calculations, theoretical results of protonated aldehyde- and diol-forms of cationic 4IC were associated with the experimental spectrum measured at pH = 2. Since the neutral diol form was experimentally not found (*vide infra*), only the neutral aldehyde form of 4IC was considered as possible model for the experimental spectrum of 4IC at pH = 5. Finally, the deprotonated aldehyde form of anionic 4IC and the neutral aldehyde form were the species considered to model the spectrum at pH 12. This pH range around p$K_{a,1}$ and p$K_{a,2}$ is used to model the protonated and deprotonated species, with the diol only present at pHs below p$K_{a,1}$, allowing the study of which speciated form of 4IC is favored at low and high pHs and what natural transition orbitals are responsible for the absorption bands.

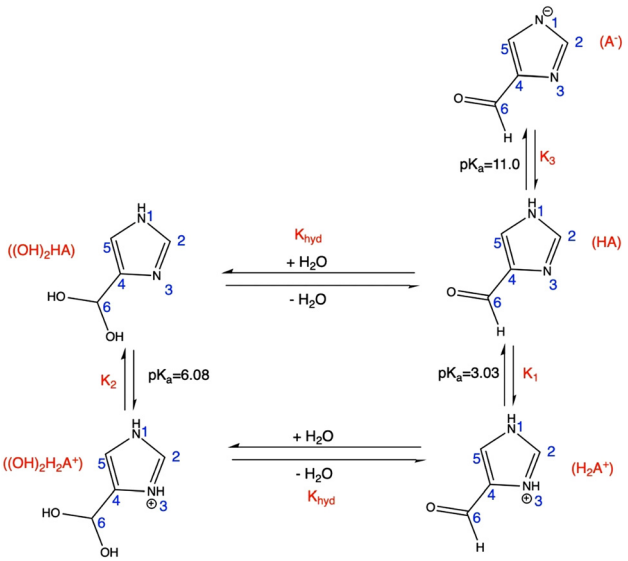

Scheme 1 The associated protonation and hydration equilibrium reactions that occur in aqueous solution for 4IC. Each species is labeled in red in which HA refers to 4-imidazolecarboxaldehyde.

Results and discussions

Experimental results

The UV-vis spectra for 100 mM solutions of 4IC at pHs 1.0 to 12.0 is shown in Fig. 1A. Under acidic conditions (pH 1.0 and 2.0), two distinct bands are evident: a less intense band at 277 nm, which shows some overlap with the solar spectral irradiance, labeled band-I, and a prominent high-energy band centered at 237 nm, labeled band II. No significant spectral changes are observed between pH 1.0 and 2.0. At pH 3.0, the higher energy band broadens, exhibiting an extended absorbance tail beyond 300 nm, which begins to overshadow the lower intensity band. By pH 4.0, a slight redshift of 8 nm is observed in band-II, with its tail extending past 300 nm. No spectroscopic evidence for the band-I is observed beyond pH 4.0. Above pH 4.0, the absorption band-II continues to redshift, accompanied by an increase in intensity, reaching a center at 256 nm at pH 5.0. Band-II remains relatively stable in both intensity and position up to pH 11.0. At pH 12.0, further redshift is observed, shifting band-II to approximately 281 nm, along with an additional increase in absorbance intensity. While only one absorption band is clearly observed above pH 11.0, the second derivative of the UV-vis spectrum (Fig. 1B) shows an additional high-energy absorption band, band-III, centered around 230 nm.

As shown in Scheme 1, while 4IC has a relatively simple structure, it can exist as a mixture of five different forms in aqueous solution, making it a complex system to study. In aqueous solution, 4IC exists in its aldehyde and its hydrate, the geminal diol 4-imidazole-2,2-dihydroxy ($(OH)_2$HA). In addition, each one of these forms also have their respective conjugate acids, where protonation at different pK_as takes place in the N3 nitrogen, as shown in Scheme 1. At higher pK_a the aldehyde form of 4IC can be further deprotonated to form a net anionic

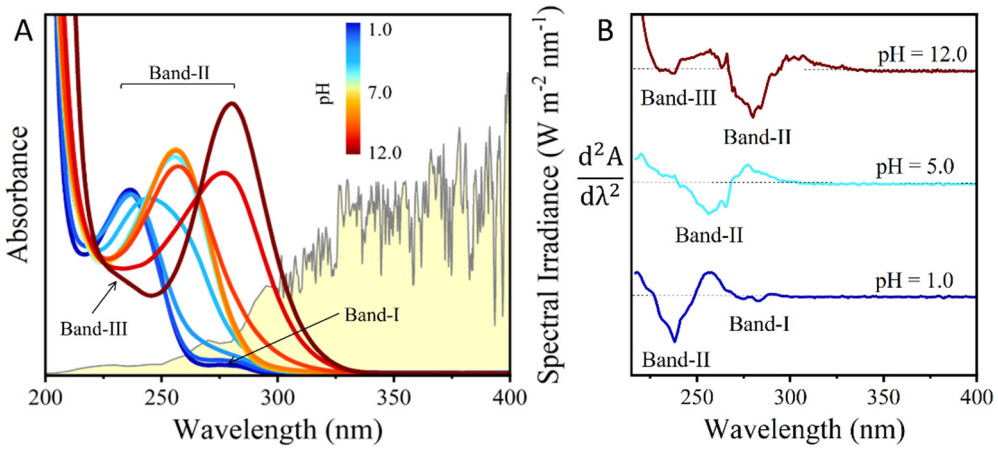

Fig. 1 (A) Absorbance spectra of a solution of 100 mM of 4IC at different pHs – in yellow: solar spectral irradiance (data from NOAA, LASP spectral solar irradiance).[47] (B) 2nd derivative of the spectrum to better identify absorption bands.

aldehyde form of 4IC. Traditional potentiometric titrations tend to overestimate the first pK_a of the aldehyde form, as the technique cannot distinguish between the aldehyde and diol species. The second pK_a is often missed or it is difficult to estimate due to a low-sensitivity transition that is difficult to detect potentiometrically (see Fig. S2). Thus, in order to determine the pK_as and the speciation of 4IC in aqueous phase, a pH-dependent ^{1}H-NMR analysis was carried out at 22 °C. This carbonyl-diol equilibrium is commonly observed in other environmentally significant chromophores. The pH ranges widely from acidic conditions (around pH 2, typical of submicron aerosols) to basic environments (around pH 8, characteristic of the MBL).[41] While the diol form is not stable isolated, its presence in solution is possible and can increase the speciation of the system.[48–50]

The formation of the geminal diol in aqueous 4IC is governed by two opposing effects. On one hand, the aromaticity of 4IC enhances the electrophilicity of the aldehyde carbon *via* induction, promoting hydration and gem-diol formation in aqueous phase.[51] However, resonance effects decrease the electrophilicity of the carbonyl carbon, redistributing the charge density and inhibiting the diol formation.[51] Solvent suppression ^{1}H-NMR analysis, shown in Fig. 2, suggests that the diol form of 4IC is favored under acidic conditions, suggesting acid-catalyzed formation of the gem-diol form, with protonation at N3 being favored due to the acidity of the system. In the acid-catalyzed hydration of 4IC, protonation of the aldehyde oxygen creates an intermediate in which the carbonyl carbon becomes more electrophilic, facilitating nucleophilic attack by water and leading to the formation of the hydrate or diol form ($(OH)_2H_2A^+$).[49,52] Fig. 2A shows an upfield shift in the ^{1}H-NMR peaks, reflecting the deprotonation of both the aldehyde and gem-diol protonated forms. The peaks assigned to the gem-diol form (highlighted in red in Fig. 2A) are detectable only below pH 5.5, whereas the aldehyde form persists across all pH values. As pH increases, protonation becomes less favorable, shifting the equilibrium toward the aldehyde form of 4IC. In Fig. 2A, the aromatic protons (2 and 5) shift closer together as pH decreases. Fig. 2B shows the shift of the aldehyde proton (6), with its singlet appearing downfield at 9.861 ppm under the

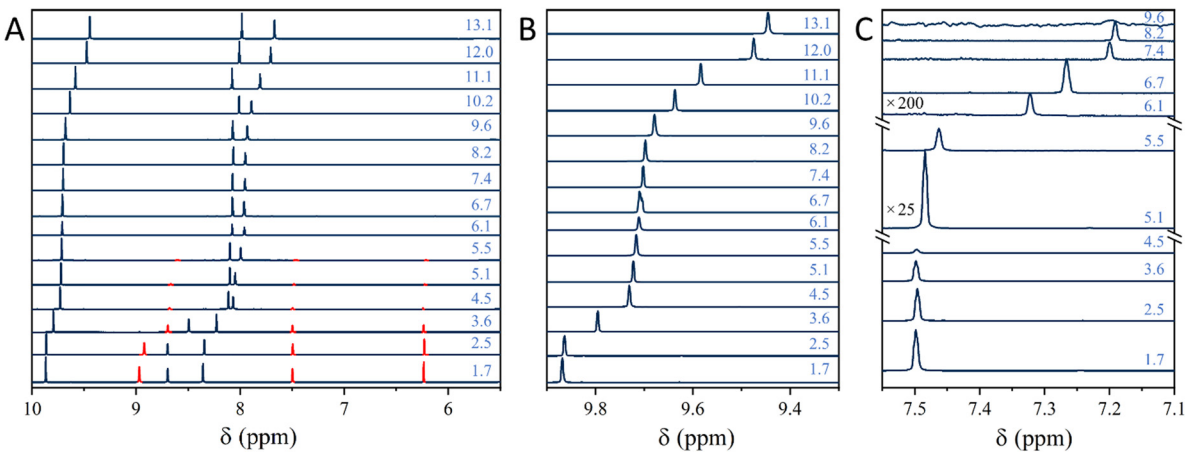

Fig. 2 ^{1}H-NMR spectra of aqueous 4IC from pH 1 to 13. pH increases from bottom to top, as it is indicated in the right side of each spectra. (A) Shift of aromatic protons (2 and 5) with the aldehyde form in black and diol form in red. (B) Shift of aldehyde proton (6). (C) Shift of nitrogen proton (1).

most acidic conditions and shifting upfield to 9.445 ppm as pH increases. In Fig. 2C, the nitrogen proton (1) is observed in the geminal diol form at low pH, transitioning to the aldehyde form as pH rises above 5.5.

Fig. 2B shows the NMR chemical shift changes with increasing pH for the proton bonded to C6 in the aldehyde form, while Fig. 2C presents the corresponding shift for the diol form. As pH increases, the signal for the diol form gradually fades, consistent with the hydration of the aldehyde being favored at lower pH. Fig. 3 shows these pH-driven changes in NMR chemical shifts plotted against pH, with the resulting titration curves enabling the calculation of the pK_a values for the aldehyde and diol forms. Calculation of the aldehyde pK_a were conducted using the ^{1}H-NMR data, through the chemical shift of the singlet peak assigned to the aldehyde form (6) and the diol pK_a by the chemical shift of the red aromatic protons (2 and 5). This chemical shift can be expressed in terms of mole fractions of the species in equilibrium, expressed here generically as HA and its conjugate base A^-:[24,50]

$$\delta_{obs} = f_{HA}\delta_{HA} + f_{A^-}\delta_{A^-} \quad (1)$$

where δ_{obs} is the observed chemical shift, and δ_{HA} and δ_{A^-} are the chemical shift of protonated and deprotonated 4IC, and f is the mole fraction expressed by eqn (2) and (3):

$$f_{HA} = \frac{[H^+]}{[H^+] + K_a} \quad (2)$$

$$f_{A^-} = \frac{K_a}{[H^+] + K_a} \quad (3)$$

The acid–base equilibrium constants, K_a, were extracted from a non-linear least-squares fitting of the experimental data δ_{obs} *vs.* pH to eqn (1)–(3), using the software package OriginPro (OriginLab), as shown in Fig. 3. In the fitting, the equilibrium constant is included as a free parameter in the model function and is determined by regression to best fit the experimental data. All pK_a values reported in Table 1 were obtained from the analysis of the ^{1}H-NMR titration data. Fig. 3A yielded the p$K_{a,1}$ of the aldehyde form, Fig. 3B the p$K_{a,2}$ of the aldehyde form, and Fig. 3C the pK_a of the diol form. There is no detected p$K_{a,2}$ for the diol form, as it is no longer observed at the pH levels required for further deprotonation of the geminal diol.

Table 1 pK_a values of 4IC, extracted from the fitting of data in Fig. 3 using eqn (1). Values were determined at a constant temperature of 22 °C under low ionic strength conditions, with a maximum estimated ionic strength of approximately 1×10^{-3} M at the highest pK_a

pK_a	Equilibrium (speciation)
3.03 ± 0.06	p$K_{a,1}$ (aldehyde form)
11.0 ± 0.1	p$K_{a,2}$ (aldehyde form)
6.08 ± 0.07	p$K_{a,1}$ (diol form)

The chemical shift fitting shown in Fig. 3 aligns well with eqn (1), yielding R^2 values of 0.995 and 0.975 for p$K_{a,1}$ and p$K_{a,2}$ in the aldehyde form of aqueous 4IC, and 0.998 for the diol form. The measured pK_as also suggest that at pHs below 4, relevant for atmospheric processing, protonated species will determine the optical properties of the chromophore. This is in good agreement with Fig. 1, which shows the disappearance of a small band (band-I) around 255 nm, either as it fades or is overlapped by the red-shifting intense band centered at 236 nm (band-II). Band-II initially shifts 9 nm as pH increases from 2 to 3, followed by an additional 10 nm shift as pH reaches 4, resulting in a total red shift from 236 nm to 255 nm as pH rises from 2 to 4, around p$K_{a,1}$ of 3.03 for the 4IC aldehyde form. In contrast, Fig. 1 shows no detectable shift as the pH increases above the p$K_{a,1}$ of the geminal diol form (6.08 ± 0.07). This is consistent with Fig. 2C, which shows a relatively strong NMR signal for the protonated diol form, while the signal for the neutral diol form gradually fades, suggesting that 4IC hydration occurs primarily at pH < 6 and, therefore, has little to no impact in the optical properties of the 4IC aqueous solution. Finally, as the pH increases over p$K_{a,2}$ of 11.0 ± 0.1, leading to the deprotonation of the 4IC aldehyde form, there is a clear red shift in the absorbance spectra of aqueous 4IC in Fig. 1 from 257 nm to 280 nm.

The equilibrium constant and subsequent speciation between aldehyde and diol form can also be calculated based off the ^{1}H-NMR spectra. The estimated hydration equilibrium

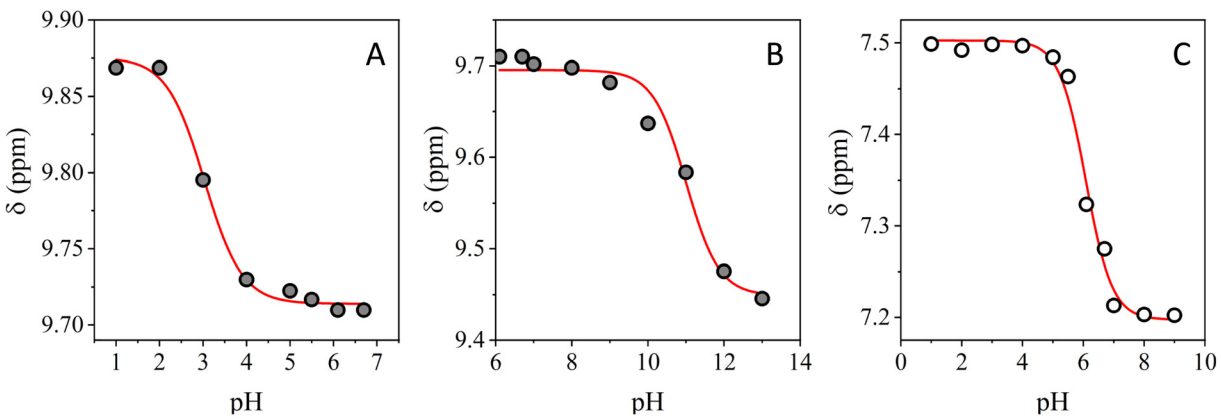

Fig. 3 (A) and (B) in gray circles, chemical shift (δ_{obs}) *vs.* pH for the aldehyde proton (9.9 to 9.4 ppm); (C) in white circles, chemical shift (δ_{obs}) *vs.* pH for the nitrogen proton (7.5 to 7.2 ppm). The red line represents the non-linear fitting to eqn (1).

constant, K_{hyd}, is the ratio of the geminal diol and aldehyde concentrations, $\frac{[diol]}{[aldehyde]}$, estimated based on the ^{1}H NMR integration of the peaks in Fig. 2. The value of K_{hyd} changes across the entire pH range of these data, consistent with an acid-catalyzed hydration, following a sigmoidal-Boltzmann model:

$$K_{hyd} = \frac{K_{hyd}^{min} + \left(K_{hyd}^{max} - K_{hyd}^{min}\right)}{1 - e^{\left(\frac{(pH - pH_0)}{dpH}\right)}} \quad (4)$$

where K_{hyd}^{min} is the lower limit of the hydration equilibrium, as determined by its asymptotic approach to zero at higher pHs. K_{hyd}^{max} is the upper boundary of the hydration equilibrium, which corresponds to the $\frac{[diol]}{[aldehyde]}$ values calculated at low pHs. Under high acidity, the maximum formation of the diol is reached, leading to quasi-steady state formation of diol and a relatively constant K_{hyd}^{max}. Finally, pH_0 is the point of transition between the upper and lower boundaries of K_{hyd}, with dpH the constant period of the pH that determines the profile. Here, pH_0 is near the value of $pK_{a,1}$ for the aldehyde form, with pH_0 = 2.98 ± 0.06. Below this pH, the concentration of neutral aldehyde is more than twelve times that of diol, indicating that most of the hydration reaction will take place on the protonated 4IC. Eqn (4) allows us to estimate the value of K_{hyd} at any pH, which can then be used to determine the speciation of 4IC with respect of pH, as shown in Fig. 4.

The ^{1}H-NMR spectra indicate that both the geminal diol and aldehyde forms are present below pH 5.5, with nearly all diol present in protonated form. The speciation diagram shown in Fig. 5 (with calculation details provided in the SI) indicates that the fraction of 4IC in neutral diol form reaches a maximum of only 0.016% at pH 3.2. At pH 1 and 2, the protonated aldehyde

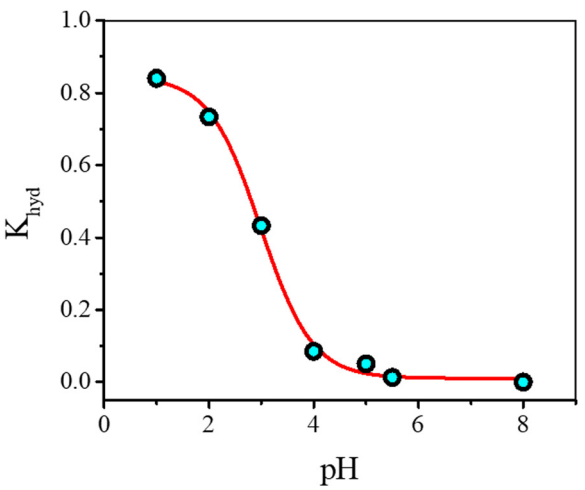

Fig. 4 Calculated hydration equilibrium constants for 4IC. K_{hyd} values are calculated as the ratio between the integrations of the diol NMR peak to that of the aldehyde. Consistent with an acid-catalyzed process, the hydration equilibrium constant decreases with pH, following a sigmoidal-Boltzmann model (red line).

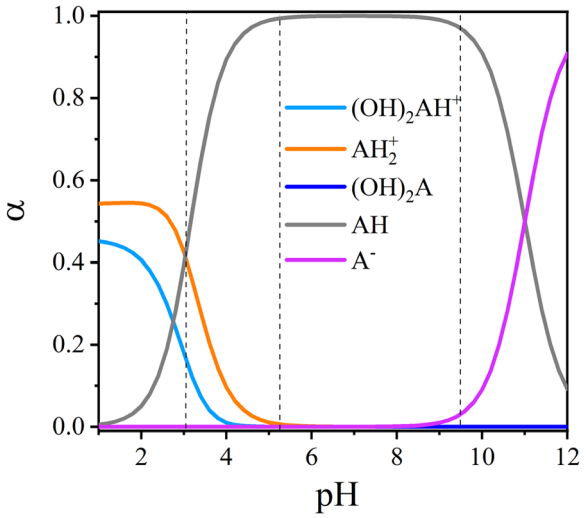

Fig. 5 Speciation of 4IC as a function of pH. Dotted lines represent the values of pK_as for the aldehyde and diol forms of 4IC.

and diol form coexist in solution and, as pH increases to 5, the aldehyde form is the prevalent species in solution with fractions above 0.99 between pH 5 and pH 9, as shown in Fig. 5. Overall, the neutral aldehyde form is the dominant form of 4IC in aqueous phase from pH 3 to 11, which is consistent with the calculated pK_a values of 3.03 and 11.0. Above pH 11, the deprotonated aldehyde becomes dominant, with a fraction at 0.91 above pH 12.

The experimentally determined pK_as and speciation calculations (Fig. 5) suggest that at pHs below 3, characteristic of submicron sea spray aerosols[41] or the aerosol deliquescent layer,[41,53–56] the dominating species of 4IC in aqueous phase will be a combination of the protonated geminal diol and the protonated aldehyde form. As pH increases above 4—typical of total suspended particles in the MBL—and approaches pH 8, characteristic of the SSML, aqueous 4IC predominantly exists in its neutral aldehyde form, which remains dominant up to pH 11. Finally, although less environmentally relevant, above pH 11 the anionic aldehyde form is the dominant species of aqueous 4IC. This speciation determination guided the time-dependent quantum chemical calculation of the small 4IC·$(H_2O)_8$ clusters to simulate the absorbance spectra in Fig. 1: the aqueous 4IC spectrum at pH 2 is best represented by a combination of the protonated geminal diol and aldehyde species, while the spectrum at pH 5 corresponds to the neutral aldehyde form. Finally, at pH 12, the absorbance spectrum is better modeled by the anionic aldehyde form of 4IC.

Comparison of the theoretical and experimental results

In general, there is a good agreement between the experimental and theoretical spectra, not only including the energy of the absorption bands, but the intensity trends and shape of the bands.

Experimental results indicate that at low pH, the acid–base equilibrium of aqueous 4IC favors the formation of both the geminal diol and aldehyde forms. To confirm this and account

for the two absorption bands observed in 4IC solutions between pH 1.0 and 3.0, theoretical models were developed using protonated aldehyde and hydrated diol complexes as representative species of 4IC under acidic conditions. The match in the optical spectra between the experiment and one of the theoretical models will allows to determine the natural transient orbitals (NTOs) and role of solvent in the electronic transition. The experimental optical absorption spectrum at pH 2 is compared to two theoretical models, a protonated aldehyde form and a geminal diol form of 4IC·$(H_2O)_8$. Each theoretical spectrum was multiplied by the mol fraction found through the experimental work for pH 2 (Fig. 5) and added together to produce the theoretical combined spectrum of the solution containing the two species, which is shown in Fig. 6A.

The spectra of the small cluster model indicate that most of the absorbance for the diol form occurs below 200 nm, outside the experimental dynamic range (200–1100 nm), except for a theoretical band at 209 nm, which may contribute to the broad absorption observed near 200 nm. Above this threshold and extending into the visible range, absorbance is primarily dominated by the protonated aldehyde form, which exhibits two bands closely resembling experimental observations: a weak, higher-energy band-I and a more intense, lower-energy broad band-II. In the theoretical spectrum of protonated aldehyde–4IC, the weak band at 258 nm, appearing as a shoulder in the combined theoretical spectrum, corresponds to the experimental band-I, while the intense high-energy band at 232 nm aligns with the experimental band-II. Overall, the small cluster model demonstrates strong agreement between experiment and theory. For band-I, both experimental and theoretical spectra show a slight tailing toward higher wavelengths, with the experimental band-I appearing slightly more redshifted at 273 nm compared to the theoretical band at 258 nm (Table 2). For the more intense band-II, the discrepancy between theoretical and experimental peak positions is minimal, with a difference of only 4 nm.

As pH increases above the p$K_{a,1}$ of the aldehyde–4IC form to pH 5, as shown in Fig. 6B, the theoretical spectra, calculated using the small cluster of the neutral aldehyde form shows a significant redshift of band-II of 28 nm, in good agreement with the experimental observations, which shows a redshift from pH 2 to pH 5 of 20 nm. At pH 5.0, the theoretical and experimental positions in band-II is also similar, with the theoretical band slightly redshifted in 4 nm (Table 2). An additional absorption band, labeled band-III, is observed as a shoulder in the theoretical spectrum, yet not observable in the experimental spectra, likely enclosed within the strong absorption near 200 nm. As pH increases above the p$K_{a,2}$ of the aldehyde–4IC form to pH 12, as shown in Fig. 6C, the small cluster of the anionic aldehyde form shows a significant redshift for band-II of 19 nm in the theoretical spectra, in good agreement with the experimental data, which shows a similar redshift of 23 nm. At pH 12, however, the experimental band-III appeared at significantly lower intensity and at lower wavelengths than the theoretical model. While TD-DFT method reproduces the high energy band-III, the intensity of the theoretical band is higher and redshifted compared to the experimental observation, as shown in Fig. 6C. As deprotonation takes place, the negative charge in

Table 2 Experimental and theoretical optical absorption spectral data for 4ICA (aldehyde form) at different pH. The term $|\Delta\lambda_{E-T}|$ indicates the absolute difference between the center of the experimental band and the theoretical band. Diol bands are not included as most of its absorption bands fall outside the experimental dynamic range

		TD-DFT Protonated 4IC·$(H_2O)_8$	
Bands	Experiment (pH 2.0) (nm)	Aldehyde-form (nm)	$\|\Delta\lambda_{E-T}\|$ (nm)
Band-I	273	258	15
Band-II	236	232	4
		TD-DFT deprotonated 4IC·$(H_2O)_8$	
Bands	Experiment (pH 5.0) (nm)	Aldehyde-form (nm)	$\|\Delta\lambda_{E-T}\|$ (nm)
Band-II	256	260	4
Band-III	n.r.	212	—
		TD-DFT deprotonated 4IC·$(H_2O)_8$	
Bands	Experiment (pH 12.0) (nm)	Aldehyde-form (nm)	$\|\Delta\lambda_{E-T}\|$ (nm)
Band-II	279	279	0
Band-III	230	242	12

n.r. = not resolved.

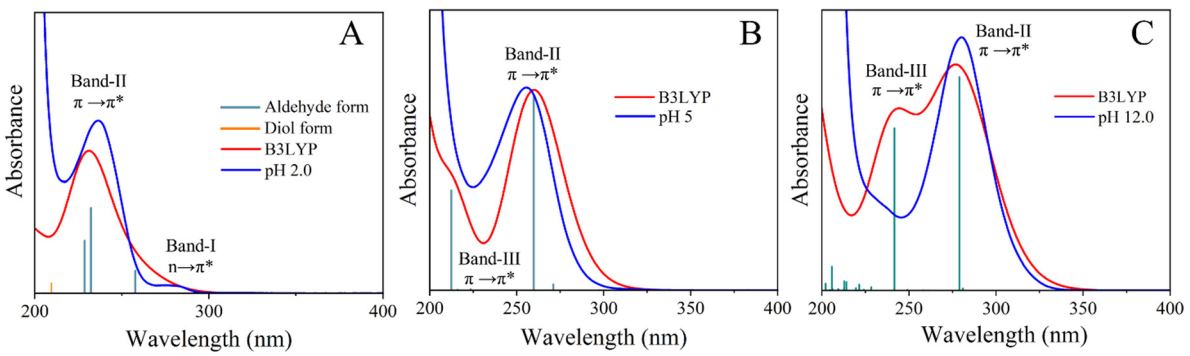

Fig. 6 Comparison of the theoretical (red line) and experimental (blue line) optical absorption spectra at different pHs. (A) pH 2.0; (B) pH 5.0; (C) pH 12.0. At pH 5.0 and 12.0, only the aldehyde form is used to simulate the spectrum. Level of theory is B3LYP/6-311++G(d,p) (gas phase). While all transitions correspond to mixed n → π* and π → π* character, the dominant transition for each band is indicated below the band designation.

4IC will cause the π orbitals in the aromatic ring to be more diffuse, demanding more solvating water molecules to stabilize the larger NTOs. The optimized anionic structure of the small cluster, denoted as $[4IC{\cdot}(H_2O)_n{\cdot}(H_2O)_m{\cdot}(H_2O)_b]^-$, reaches a global minimum with $n = 3$, representing water molecules around the aldehyde group, $m = 4$ interacting with the aromatic ring, and $b = 1$ bridging the two regions. This global minimum structure (Fig. S1) corresponds to the spectrum in Fig. 6B, which features a highly intense and redshifted band-III. To explore alternative local minima, additional models were tested (see Fig. S3) by gradually redistributing water molecules to increase solvation around the diffused aromatic ring, resulting in two structures: one with $n = 3$, $m = 5$ and another with $n = 2$, $m = 6$, both with $b = 0$. The increase in solvation of the aromatic π orbitals in 4IC has a minimum effect on band-II, causing a slight blue shift with the addition of water molecules in the solvation shell around the aromatic ring. Band-III undergoes a total blue shift of 10 nm while also decreasing in intensity, bringing it into closer agreement with the experimental spectrum. This theoretical observation suggests that a larger cluster may be needed to more accurately simulate diffuse orbitals and anionic systems. While the small cluster still models well the general features of the absorbance spectra of 4IC, the limitation in simulating diffuse molecular orbitals is less pronounced under the acidic conditions of aerosol particles or the slight basicity of the SSML, where these effects are less pronounced. These computational studies suggest that, for the anionic form of 4IC, the redistribution of surrounding water molecules plays a significant role in shaping the calculated spectral features, suggesting that larger water clusters could further improve the accuracy of simulations for anionic systems. Yet, the current small-cluster model provides strong agreement with experimental spectra, even at high pH, well within the deviations reported for similar systems.[25,26,34] This suggests that the approach is well-suited to simulate environmentally relevant chromophores and effectively captures the energy transitions observed experimentally.

Fig. 6 also shows a general trend in absorption band-II of aqueous 4IC as pH increases: a redshift in this most intense absorption band is accompanied by an increase in its absorbance intensity. As the pH increases across p$K_{a,1}$, from pH 2 to pH 5, the red shifting band-II becomes significantly more intense, with a ratio of the experimental intensities (I_{pH}^{exp}) for band-II at pH 2 to pH 5 of $\frac{I_{pH=2}^{exp}}{I_{pH=5}^{exp}} = 0.84$. The theoretical spectrum also undergoes a similar increase in intensity (I_{pH}^{Th}), with a ratio of $\frac{I_{pH=2}^{Th}}{I_{pH=5}^{Th}} = 0.74$. As pH continues to increase to pH 12, another significant increase in absorption intensity takes place in the experimental spectra, with a ratio of the intensities for band-II at pH 5 to pH 12 of $\frac{I_{pH=5}^{exp}}{I_{pH=12}^{exp}} = 0.81$, in good agreement with the theoretical increase in intensity of $\frac{I_{pH=5}^{Th}}{I_{pH=12}^{Th}} = 0.89$. Overall, Fig. 6 and Table 2 show good agreement between the theoretically calculated spectra and the experimentally obtained absorbances, in particular in transition energy – as indicated by the absolute difference between the center of the experimental band and the theoretical band $|\Delta\lambda_{E-T}|$ – but also in the relative intensity of the experimental and theoretical absorption bands.

Spectral changes in Fig. 1 and summarized in Fig. 6 suggest that the increase in pH—which suppresses the hydration of 4IC and leads to its overall deprotonation—also brings about two effects that together result in a net redshift of band-II, the disappearance of band-I, and the rise of a third absorption band. First, increased electron delocalization lowers the electronic transition energy, causing a redshift in the absorption spectrum. Second, favorable interactions between water and 4IC species tend to stabilize the ground states, which increases the electronic transition energy, resulting in a blueshift. At low pH, protonated 4IC—whether in its diol or aldehyde form—undergoes a cation–dipole interaction with water that stabilizes its ground state, increasing the energy required for the transition to the excited state and resulting in a blue shift. As pH increases and more neutral 4IC is formed, this interaction becomes less favorable, leading to a less stabilized ground state and a redshift as pH increases. Additionally, protonated 4IC has fewer resonance structures than its neutral counterpart, as zwitterionic resonance forms are not favored in the cationic state (Scheme S1). With increasing pH, the neutral form of 4IC gains additional resonance structures, enhancing electron delocalization and further lowering the electronic transition energy. Collectively, these effects contribute to the overall redshift in band-II observed in the absorption spectrum in Fig. 6 in the spectra at pH 2 and pH 5.

The neutral form of 4IC, dominated by the aldehyde form between pHs 4 and 11, has at least seven resonance structures in the aromatic ring (Scheme S1), slightly more than the six resonance structures of the anionic form of aldehyde–4IC. However, this delocalization favors the negative charge of the anion shifting toward the oxygen in the aldehyde group, effectively distributing the charge without forming zwitterions. This increased delocalization leads to a redshift in the absorption spectrum as the pH rises to 12. Although the interaction between water and the more polar anionic 4IC is relatively stronger, stabilizing the ground state of the deprotonated species at pH 12 compared to the neutral form, this solvent effect slightly increases the electron transition energy, resulting in a minor blueshift. However, this effect is not as pronounced, and the overall trend remains a redshift with increasing pH.

Fig. 7–9 show the hole-particle NTOs involved in the electronic transitions of the protonated, neutral, and deprotonated clusters of the aldehyde form of 4IC. These figures also report the corresponding excitation energies, oscillator strengths, and the molecular orbitals for the transition. At all pH values, the absorption bands of the aldehyde form of 4IC—including the low-energy band-I, the more intense higher-energy band-II, and band-III (which emerges at higher pH)—originate from a combination of n → π* and π → π* transitions. In all cases, the nitrogen lone pair contributes to the vertical excitation of

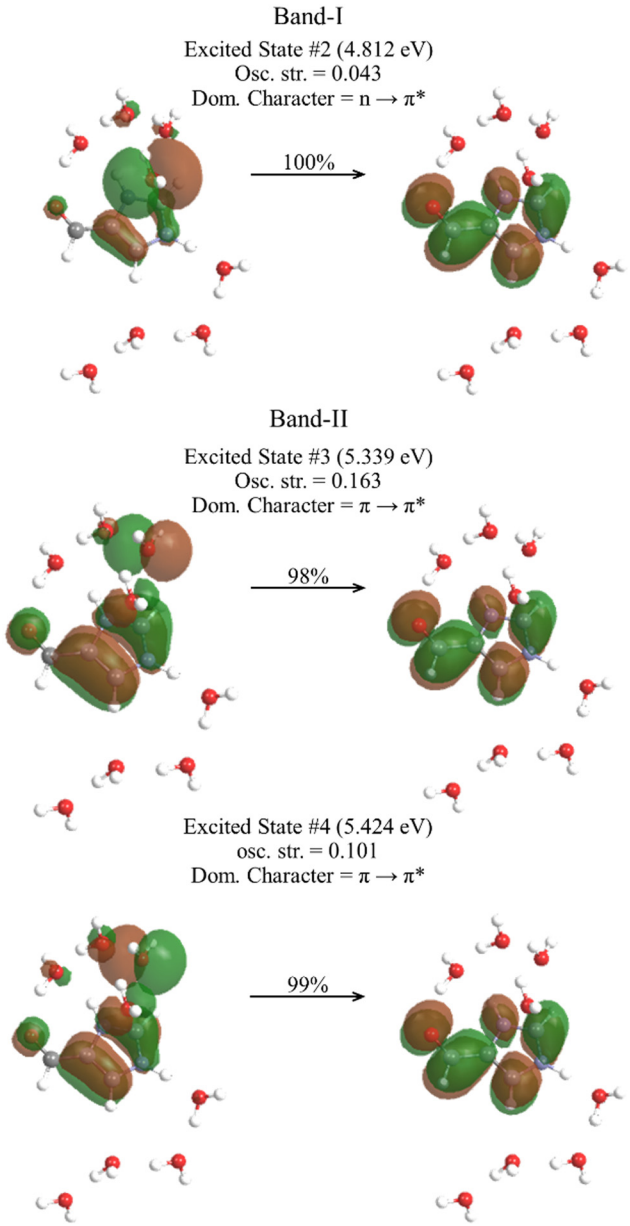

Fig. 7 Natural transition orbitals of the selected excited states of protonated aldehyde-form of 4IC·$(H_2O)_8$ calculated at the B3LYP/6-311++G(d,p) (gas phase).

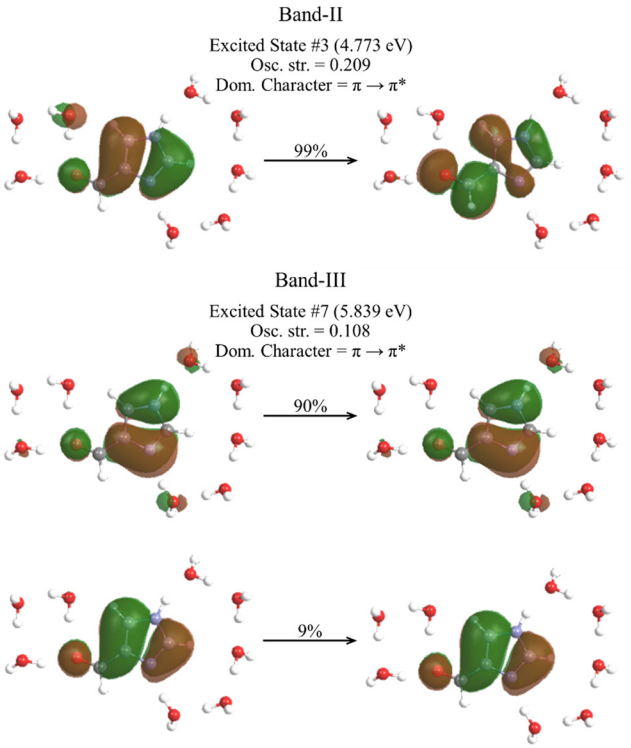

Fig. 8 Natural transition orbitals of the selected excited states of neutral aldehyde-form of 4IC·$(H_2O)_8$ calculated at the B3LYP/6-311++G(d,p) (gas phase).

the aldehyde species in aqueous solution. However, there are subtle differences that impact the spectral features of aqueous 4IC. At low pHs (Fig. 7) the HOMO orbitals for the protonated 4IC involve the water molecules. This suggests that both 4IC and the surrounding water molecules contribute to the electronic transitions observed in band I and band II. In particular, the orbitals of water molecules interacting with the aromatic ring of 4IC play a more significant role in band II. In contrast, the modeled LUMO states show no involvement of water orbitals across all forms of the aldehyde—protonated, neutral, and deprotonated—indicating that water primarily stabilizes the ground state rather than the excited state. This stabilization increases the energy gap between ground and excited states, leading to a blueshift in absorption. At low pH, the protonated form of 4IC exhibits stronger water orbital contributions due to cation–dipole interactions, further highlighting the importance of explicitly modeling solvation when investigating the chromophore's optical properties. At low pH, the electronic transition retains a nodal point between the aldehyde carbon (C6) and the rest of the molecule, with the excited state shifting the nodal point to include delocalization in C6, suggesting a limited delocalization in both the ground and excited states. This reduces the spectral impact of electron delocalization, as both states involved in the transition are similarly constrained by the nodal point. The presence of this nodal point reflects the structural tendency of the carbonyl group: under acidic conditions, nucleophilic attack favors diol formation, rather than maintaining an open carbonyl that could support conjugation with the aromatic ring. As a result, resonance between the aldehyde and the ring is less likely, making extended delocalization—and its corresponding spectral signature—less prominent (Scheme S1).

As pH increases, the effect of water molecular orbitals in the electronic transition decreases. In particular, for the neutral aldehyde-form of 4IC, the cation–dipole interaction that stabilized the ground state of the protonated 4IC is no longer present. However, the participation of water orbitals is still observed in the HOMO orbital for band-II and pH 5, in one of the water molecules that solvates the aldehyde group of 4IC, as shown in Fig. 8. Thus, with respect to low pHs, the role of water solvation in the stabilization of the ground state is lower for the

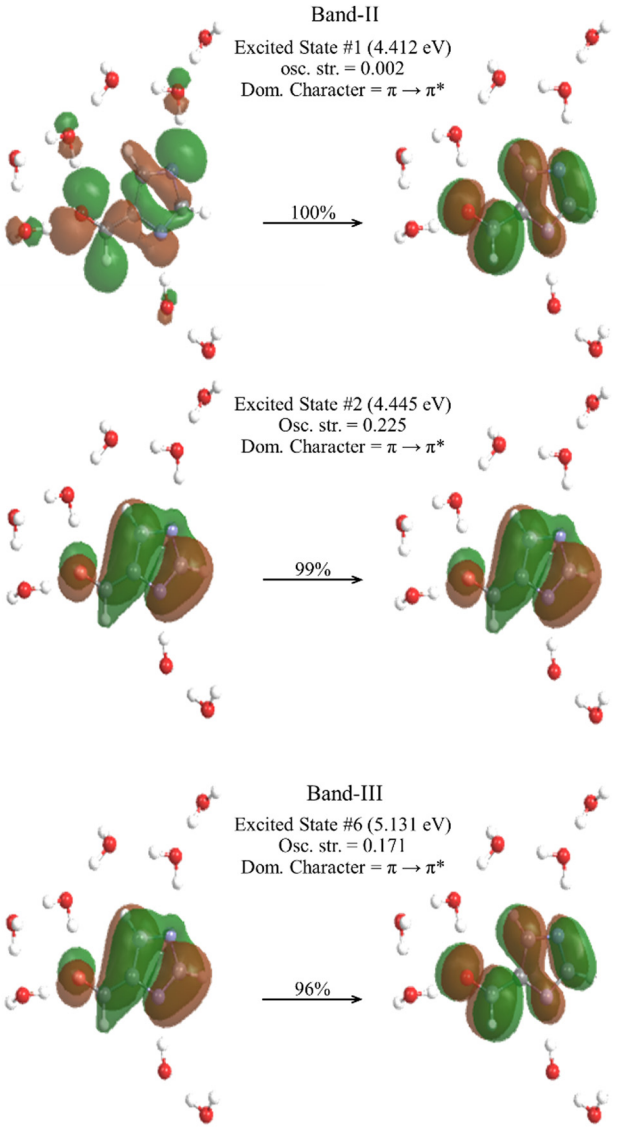

Fig. 9 Natural transition orbitals of the selected excited states of deprotonated aldehyde-form of 4IC·$(H_2O)_8$ calculated at the B3LYP/6-311++G(d,p) (gas phase).

neutral 4IC cluster, resulting in a decrease in the energy gap between ground and excited states, leading to a redshift in absorption as pH increases, as shown in Fig. 1. For band-III, some molecular orbitals from the water molecules solvating the aromatic ring are participating in the NTO with higher probability, suggesting some level of water effect in the electronic transition.

Finally, in the fully deprotonated aldehyde form of 4IC, band II is primarily associated with an n → π* transition localized on the carbonyl group, while π → π* transitions dominate within the aromatic ring. This suggests that resonance structures involving partial delocalization into the carbonyl group become more favorable, enhancing conjugation in the ground state. The increased delocalization also stabilizes the excited state, leading to a redshift in the absorption as pH increases, as shown in Fig. 1. While this structure also shows a ground state stabilization *via* ion–dipole interactions, the higher amount of resonance structures plays a significant role stabilizing the excited state and decreasing the electron transition, with the concomitant redshift.

Based on NTO analysis, all excitations observed in 4IC·$(H_2O)_8$ clusters are the result of mixed n → π*/π → π* transitions. In nearly all cases, the dominant transition is π → π*, with band I having a dominant n → π* character, as summarized in Table 3.

Combining theoretical calculations with experimental observations shows that, at low pH, the optical spectra of aqueous 4IC below the solar radiation cutoff (290 nm) is dominated by the protonated aldehyde form. Additional contributions from the protonated diol form appear primarily at wavelengths ≤ 210 nm—well below the range of solar actinic flux. Although the protonated diol form absorbs outside the relevant solar range, it still influences the overall absorbance by decreasing the concentration of the aldehyde form through acid-favored hydration. Moreover, diol formation disrupts resonance involving the carbonyl group, limiting electron delocalization and, consequently, the stabilization of the excited state. Similarly, the theoretical spectra of the neutral and deprotonated aldehyde forms accurately reproduce the experimental spectra at pH 5 and pH 11, respectively, modeling the redshift observed as pH increases. The calculations confirm that the increased electron delocalization in the deprotonated aldehyde form at higher pH results in a slight decrease in excitation energy, consistent with the redshift shown in Fig. 1. While the theoretical spectrum of the deprotonated aldehyde form of 4IC correctly models the direction of the spectral shift with pH, the energies of the absorption bands, and the relative band intensities across systems, it slightly overestimates the absolute intensity of band-III for the deprotonated species at high pH. This discrepancy likely arises from challenges in modeling solvent effects for anionic species using a small cluster approach. Although using larger clusters could further improve agreement, the small cluster TD-DFT shown here already provides promising predictive method for nitrogen-containing chromophores in aqueous environments.

Table 3 Summary of calculated transitions for 4ICA (aldehyde form) at different pH. All transitions in 4IC·$(H_2O)_8$ clusters exhibit mixed n → π*/π → π* character. Classifications indicate the dominant contribution based on NTO analysis while acknowledging this mixing

System	Band	Excited state	Energy, eV (nm)	Osc. strength	Dominant character
Protonated	Band-I	2	4.812 (258)	0.043	n → π*
	Band-II	3	5.339 (232)	0.163	π → π*
	Band-II	4	5.424 (229)	0.101	π → π*
Neutral	Band-II	3	4.773 (260)	0.209	π → π*
	Band-III	7	5.839 (212)	0.108	π → π*
Deprotonated	Band-II	1	4.412 (281)	0.002	π → π*
	Band-II	2	4.445 (279)	0.225	π → π*
	Band-III	6	5.131 (242)	0.171	π → π*

Conclusions and atmospheric implications

In this work, spectroscopic measurements are combined with theoretical calculations to investigate the optical absorption spectra of 4IC in aqueous solution. The hydration equilibrium and acid–base speciation of 4IC were characterized using ^{1}H NMR spectroscopy, which allowed quantification of the relative amounts of the diol and aldehyde forms as a function of pH and enabled experimental determination of pK_a values. Our results show that the hydration of 4IC is acid-catalyzed, and that aqueous-phase 4IC exists as a mixture of protonated diol and aldehyde species under acidic conditions. The pK_a values of the aldehyde form were determined to be 3.03 ± 0.06 and 11.0 ± 0.1, corresponding to its transitions from protonated to neutral and neutral to deprotonated forms, respectively. The diol form was only detected at low pH, with a pK_a of 6.08 ± 0.07. The pK_as reported suggest that 4IC is slightly weaker as an acid than its isomer 2IC,[40] suggesting that fractions of aerosol particles containing 4IC will remain protonated through the SSA submicron regime, with the concomitant hydration and formation of the diol form. Theoretical calculations using a small water cluster model showed good agreement with the experimental spectra. At low pH, band I appears experimentally at 273 nm and is predicted at 258 nm by TD-DFT, while band II is observed at 236 nm and calculated at 232 nm. As the pH increases to conditions where the neutral aldehyde form of 4IC dominates, band II undergoes a redshift of 20 nm experimentally and 28 nm in our TD-DFT simulations, with a theoretically observed band-III showing at higher-energies at 212 nm. Finally, at pH 12.0, where the fully deprotonated aldehyde form of 4IC is predominant, bands II and III continue the redshift trend observed with increasing pH. Experimentally, band II shifts by 23 nm, while TD-DFT predicts a shift of 19 nm. Band III, which is only observed theoretically at pH 5.0, shifts by 28 nm.

Quantum chemical calculations indicate that the absorbance features shown in Fig. 1 arise from electronic transitions of the aldehyde form of 4IC, primarily due to n → π* and π → π* transitions. The diol form, relevant only at low pH values such as those found in submicron SSA, exhibits high-energy absorption bands that fall outside the solar actinic flux and therefore do not directly contribute to 4IC's optical properties under solar irradiation. However, the diol form indirectly affects the absorbance of the aldehyde form at low pH in two important ways. First, the concentration of the light-absorbing aldehyde form decreases, as a substantial fraction of 4IC exists in the diol form—exceeding 40% at pH 2.0 and below. Second, diol formation disrupts conjugation with the carbonyl group, limiting electron delocalization and resulting in electronic transitions that are more influenced by ground-state stabilization through cation–dipole interactions. At higher pHs, such as those found for total suspended SSA and the SSML, the absorbance features of 4IC correspond to electronic transitions for the neutral aldehyde form. Analysis of the excited-state orbitals in the cluster models shows that the prominent absorbance feature, band II, arises from transitions involving both 4IC and nearby water molecules. By combining quantum chemical calculations with cluster-based solvation models, we gain molecular-level insight into the absorption behavior of 4IC in aqueous environments. This approach demonstrates that the simplified cluster approaches usefully used for other chromophores[24,25,27] can effectively interpret experimental spectra of nitrogen-containing organic compounds in water. The physicochemical properties of 4IC discussed here position it as a promising proxy for marine aerosol photosensitizers, partially contributing to the development of molecular models that enable a more quantitative assessment of photochemistry in the marine atmosphere.[36]

Author contributions

Conceptualization of the study: J. G. N. method development: L. W., E. S., and J. G. N. measurements: E. S., C. C., and L. W. data analysis: all. Discussion: all. Interpretation of results: E. S., L. W., and J. G. N. writing – original draft: E. S., and J. G. N. final editing: J. G. N.

Conflicts of interest

There are no conflicts to declare.

Data availability

All data generated or analyzed during this study are included in this published article and its SI. Raw data are available upon reasonable request from the corresponding author.

Geometrical structures of hydrated 4IC molecules, potentiometric titration, speciation calculation, local minima of the anionic structure, and resonance structures for 4IC in the aldehyde form. See DOI: **https://doi.org/10.1039/d5cp01553g**

Acknowledgements

This work was supported by the National Science Foundation through grant CHE-2003814 and by the MERCURY consortium (**https://mercuryconsortium.org/**) under NSF grants CHE-1229354 and CHE-1662030. The authors would like to thank Dr Vicki H. Grassian, Dr Michael Alves, Dr R. Benny Gerber, and Dr Jessada Mahatthananchai for helpful discussions. J. G. N. acknowledges support from the Henry Dreyfus Teacher-Scholar Awards Program.

References

1 K. Mopper and R. G. Zika, Natural Photosensitizers in Sea Water: Riboflavin and Its Breakdown Products, *Photochemistry of Environmental Aquatic Systems American Chemical Society*, 1987, p. 327.
2 E. M. Thurman, *Organic Geochemistry of Natural Waters*, Springer, Netherlands, Dordrecht, 1985.

3 N. V. Karimova, M. Luo, V. H. Grassian and B. R. Gerber, Toward a Microscopic Model of Light Absorbing Dissolved Organic Compounds in Aqueous Environments: Theoretical and Experimental Study, *Phys. Chem. Chem. Phys.*, 2021, **23**, 10487–10497.

4 J. Borgatta and J. G. Navea, Fate of Aqueous Iron Leached from Tropospheric Aerosols during Atmospheric Acidic Processing: Study of the Effect of Humic-Like Substances, *WIT Trans. Ecol. Environ.*, 2015, **198**, 155–166.

5 R. Zhang, I. Suh, J. Zhao, D. Zhang, E. C. Fortner, X. Tie, L. T. Molina and M. J. Molina, Atmospheric New Particle Formation Enhanced by Organic Acids, *Science*, 2004, **304**, 1487.

6 H. M. Ricker, A. Leonardi and J. G. Navea, Reduction and Photoreduction of NO2 in Humic Acid Films as a Source of HONO, ClNO, N2O, NOX, and Organic Nitrogen, *ACS Earth Space Chem.*, 2022, **6**, 3066–3077.

7 J. G. Navea and V. H. Grassian, Photochemistry of Atmospheric Particles. In Reference Module in Chemistry, *Molecular Sciences and Chemical Engineering*, Elsevier, 2018.

8 A. Leonardi, H. M. Ricker, A. G. Gale, B. T. Ball, T. T. Odbadrakh, G. C. Shields and J. G. Navea, Particle Formation and Surface Processes on Atmospheric Aerosols: A Review of Applied Quantum Chemical Calculations, *Int. J. Quantum Chem.*, 2020, **120**, e26350.

9 M. A. Young, *Environmental Photochemistry in Surface Waters*. 2005.

10 D. J. Hassett, M. S. Bisesi and R. Hartenstein, Bactericidal action of humic acids, *Soil Biol. Biochem.*, 1987, **19**, 111–113.

11 M. Klavins and O. Purmalis, Humic substances as surfactants, *Environ. Chem. Lett.*, 2010, **8**, 349–354.

12 J. A. Rice and P. MacCarthy, Statistical evaluation of the elemental composition of humic substances, *Org. Geochem.*, 1991, **17**, 635–648.

13 M. R. Alves, E. K. Coward, D. Gonzales, J. S. Sauer, K. J. Mayer, K. A. Prather and V. H. Grassian, Changes in light absorption and composition of chromophoric marine-dissolved organic matter across a microbial bloom, *Environ. Sci.: Processes Impacts*, 2022, **24**, 1923–1933.

14 J. S. Sauer, K. J. Mayer, C. Lee, M. R. Alves, S. Amiri, C. J. Bahaveolos, E. B. Franklin, D. R. Crocker, D. Dang, J. Dinasquet, L. A. Garofalo, C. P. Kaluarachchi, D. B. Kilgour, L. E. Mael, B. A. Mitts, D. R. Moon, A. N. Moore, C. K. Morris, C. A. Mullenmeister, C. Ni, M. A. Pendergraft, D. Petras, R. M. C. Simpson, S. Smith, P. R. Tumminello, J. L. Walker, P. J. DeMott, D. K. Farmer, A. H. Goldstein, V. H. Grassian, J. S. Jaffe, F. Malfatti, T. R. Martz, J. H. Slade, A. V. Tivanski, T. H. Bertram, C. D. Cappa and K. A. Prather, The Sea Spray Chemistry and Particle Evolution study (SeaSCAPE): overview and experimental methods, *Environ. Sci.: Processes Impacts*, 2022, **24**, 290–315.

15 J. V. Trueblood, X. Wang, V. W. Or, M. R. Alves, M. V. Santander, K. A. Prather and V. H. Grassian, The Old and the New: Aging of Sea Spray Aerosol and Formation of Secondary Marine Aerosol through OH Oxidation Reactions, *ACS Earth Space Chem.*, 2019, **3**, 2307–2314.

16 J. V. Trueblood, M. R. Alves, D. Power, M. V. Santander, R. E. Cochran, K. A. Prather and V. H. Grassian, Shedding Light on Photosensitized Reactions within Marine-Relevant Organic Thin Films, *ACS Earth Space Chem.*, 2019, **3**, 1614–1623.

17 G. Freeman-Gallant, E. J. Davis, E. Scholer, O. Alija and J. G. Navea, Photooxidation of Nonanoic Acid by Molecular and Complex Environmental Photosensitizers, *J. Phys. Chem. A*, 2024, **128**, 9792–9803.

18 S. L. Mora García, I. Gutierrez, J. V. Nguyen, J. G. Navea and V. H. Grassian, Enhanced HONO Formation from Aqueous Nitrate Photochemistry in the Presence of Marine Relevant Organics: Impact of Marine-Dissolved Organic Matter (m-DOM) Concentration on HONO Yields and Potential Synergistic Effects of Compounds within m-DOM, *ACS Environ. Sci. Technol. Air*, 2024, **1**(6), 525–535.

19 S. L. Mora Garcia, S. Pandit, J. G. Navea and V. H. Grassian, Nitrous Acid (HONO) Formation from the Irradiation of Aqueous Nitrate Solutions in the Presence of Marine Chromophoric Dissolved Organic Matter: Comparison to Other Organic Photosensitizers, *ACS Earth Space Chem.*, 2021, **5**, 3056–3064.

20 D. Kwon, M. J. Sovers, V. H. Grassian, P. D. Kleiber and M. A. Young, Optical Properties of Humic Material Standards: Solution Phase and Aerosol Measurements, *ACS Earth Space Chem.*, 2018, **2**, 1102–1111.

21 S. Jayalath, H. Wu, S. C. Larsen and V. H. Grassian, Surface Adsorption of Suwannee River Humic Acid on TiO2 Nanoparticles: A Study of pH and Particle Size, *Langmuir*, 2018, **34**, 3136–3145.

22 Y. Miyazaki, Y. Yamashita, K. Kawana, E. Tachibana, S. Kagami, M. Mochida, K. Suzuki and J. Nishioka, Chemical transfer of dissolved organic matter from surface seawater to sea spray water-soluble organic aerosol in the marine atmosphere, *Sci. Rep.*, 2018, **8**, 14861.

23 M. V. Santander, J. M. Schiffer, C. Lee, J. L. Axson, M. J. Tauber and K. A. Prather, Factors controlling the transfer of biogenic organic species from seawater to sea spray aerosol, *Sci. Rep.*, 2022, **12**, 3580.

24 D. Shemesh, M. Luo, V. H. Grassian and R. B. Gerber, Absorption spectra of pyruvic acid in water: insights from calculations for small hydrates and comparison to experiment, *Phys. Chem. Chem. Phys.*, 2020, **22**, 12658–12670.

25 N. V. Karimova, M. Luo, I. Sit, V. H. Grassian and R. B. Gerber, Absorption Spectra and the Electronic Structure of Gallic Acid in Water at Different pH: Experimental Data and Theoretical Cluster Models, *J. Phys. Chem. A*, 2022, **126**, 190–197.

26 N. Karimova, O. Alija, S. L. Mora García, V. H. Grassian, R. B. Gerber and J. G. Navea, pH Dependence of the speciation and optical properties of 4-benzoylbenzoic acid, *Phys. Chem. Chem. Phys.*, 2023, **25**, 17306–17319.

27 M. Luo, D. Shemesh, M. N. Sullivan, M. R. Alves, M. Song, R. B. Gerber and V. H. Grassian, Impact of pH and NaCl and CaCl2 Salts on the Speciation and Photochemistry of Pyruvic Acid in the Aqueous Phase, *J. Phys. Chem. A*, 2020, **124**, 5071–5080.

28 Y. Chin, G. Aiken and E. O'Loughlin, Molecular Weight, Polydispersity, and Spectroscopic Properties of Aquatic Humic Substances, *Environ. Sci. Technol.*, 1994, **28**, 1853–1858.
29 K. Kumada, Absorption spectra of humic acids, *Soil Sci. Plant Nutr.*, 1955, **1**, 29–30.
30 X. Lei, J. Pan and A. Devlin, Characteristics of Absorption Spectra of Chromophoric Dissolved Organic Matter in the Pearl River Estuary in Spring, *Remote Sens.*, 2019, **11**, 1533–1548.
31 J. Ma, R. Del Vecchio, K. S. Golanoski, E. S. Boyle and N. V. Blough, Optical Properties of Humic Substances and CDOM: Effects of Borohydride Reduction, *Environ. Sci. Technol.*, 2010, **44**, 5395–5402.
32 M. Peacock, C. Evans, N. Fenner, C. Freeman, R. Gough, T. Jones and I. Lebron, UV-visible absorbance spectroscopy as a proxy for peatland dissolved organic carbon (DOC) quantity and quality: Considerations on wavelength and absorbance degradation, *Environ. Sci.: Processes Impacts*, 2014, **16**, 1445–1461.
33 H. E. Reader, C. A. Stedmon, N. J. Nielsen and E. S. Kritzberg, Mass and UV-visible spectral fingerprints of dissolved organic matter: sources and reactivity, *Front. Mar. Sci.*, 2015, **2**, 88.
34 N. Karimova, M. Luo, V. Grassian and R. Gerber, Absorption Spectra of Benzoic Acid in Water at Different pH and in the Presence of Salts: Insights from the Integration of Experimental Data and Theoretical Cluster Models, *Phys. Chem. Chem. Phys.*, 2020, **22**, 5046–5056.
35 N. Ferdousi-Rokib, K. A. Malek, K. Gohil, K. R. Pitta, D. D. Dutcher, T. M. Raymond, M. A. Freedman and A. Asa-Awuku, Salting out and nitrogen effects on cloud-nucleating ability of amino acid aerosol mixtures, *Environ. Sci.: Atmos.*, 2025, **5**, 485–501.
36 J. P. D. Abbatt and A. R. Ravishankara, Opinion: Atmospheric multiphase chemistry: past, present, and future, *Atmos. Chem. Phys.*, 2023, **23**, 9765–9785.
37 X. Liu, H. Wang, F. Wang, S. Lv, C. Wu, Y. Zhao, S. Zhang, S. Liu, X. Xu, Y. Lei and G. Wang, Secondary Formation of Atmospheric Brown Carbon in China Haze: Implication for an Enhancing Role of Ammonia, *Environ. Sci. Technol.*, 2023, **57**, 11163–11172.
38 M. Teich, M. Schmidtpott, D. van Pinxteren, J. Chen and H. Herrmann, Separation and quantification of imidazoles in atmospheric particles using LC–Orbitrap-MS, *J. Sep. Sci.*, 2020, **43**, 577–589.
39 R. Zhao, A. K. Y. Lee, L. Huang, X. Li, F. Yang and J. P. D. Abbatt, Photochemical processing of aqueous atmospheric brown carbon, *Atmos. Chem. Phys.*, 2015, **15**, 6087–6100.
40 J. M. Ackendorf, M. G. Ippolito and M. M. Galloway, pH Dependence of the Imidazole-2-carboxaldehyde Hydration Equilibrium: Implications for Atmospheric Light Absorbance, *Environ. Sci. Technol. Lett.*, 2017, **4**, 551–555.
41 K. J. Angle, D. R. Crocker, R. M. C. Simpson, K. J. Mayer, L. A. Garofalo, A. N. Moore, S. L. Mora Garcia, V. W. Or, S. Srinivasan, M. Farhan, J. S. Sauer, C. Lee, M. A. Pothier, D. K. Farmer, T. R. Martz, T. H. Bertram, C. D. Cappa, K. A. Prather and V. H. Grassian, Acidity across the interface from the ocean surface to sea spray aerosol, *Proc. Natl. Acad. Sci. U. S. A.*, 2021, **118**, e2018397118.
42 K. J. Angle, V. H. Grassian and A. P. Ault, The rapid acidification of sea spray aerosols, *Phys. Today*, 2022, **75**, 58–59.
43 A. D. Becke, Density-functional thermochemistry. III. The role of exact exchange, *J. Chem. Phys.*, 1993, **98**, 5648–5652.
44 S. Grimme, Semiempirical GGA-Type Density Functional Constructed with a Long-Range Dispersion Correction, *J. Comput. Chem.*, 2006, **27**, 1787–1799.
45 M. C. Almandoz, M. I. Sancho and S. E. Blanco, Spectroscopic and DFT study of solvent effects on the electronic absorption spectra of sulfamethoxazole in neat and binary solvent mixtures, *Spectrochim. Acta, Part A*, 2014, **118**, 112–119.
46 D. Porezag, T. Frauenheim, T. Köhler, G. Seifert and R. Kaschner, Construction of tight-binding-like potentials on the basis of density-functional theory: Application to carbon, *Phys. Rev. B: Condens. Matter Mater. Phys.*, 1995, **51**, 12947–12957.
47 O. Coddington, J. L. Lean, C. Lindholm and P. Pilewskie, NOAA Climate Data Record (CDR) of NASA NOAA LASP Spectral Solar Irradiance (NNLSSI), Version 3, NOAA National Centers for Environmental Information, 2024, DOI: 10.25921/esjz-1w61. Accessed 2025.
48 A. F. Crespi and J. M. Lázaro-Martínez, Can a gem-Diol Moiety Be Isolated? A Reaction Study by NMR and X-ray Spectroscopies, *J. Chem. Educ.*, 2023, **100**, 4536–4542.
49 A. Parandaman, M. Kumar, J. S. Francisco and A. Sinha, Organic Acid Formation from the Atmospheric Oxidation of Gem Diols: Reaction Mechanism, Energetics, and Rates, *J. Phys. Chem. A*, 2018, **122**, 6266–6276.
50 R. J. Rapf, M. R. Dooley, K. Kappes, R. J. Perkins and V. Vaida, pH Dependence of the Aqueous Photochemistry of α-Keto Acids, *J. Phys. Chem. A*, 2017, **121**, 8368–8379.
51 S. J. Gumbley and R. Stewart, Effect of substituents at the 5-position on the first and second dissociation constants of isophthalic acid, *J. Chem. Soc., Perkin Trans. 2*, 1984, 529–531.
52 W. Knoche, M. Arturo Lopez-Quintela and J. Weiffen, The Hydration of Aliphatic Aldehydes and Pyruvic Acid in Mixed Solvents, *Ber. Bunsen-Ges. Phys. Chem.*, 1985, **89**, 1047–1050.
53 C. R. Usher, A. E. Michel and V. H. Grassian, Reactions on mineral dust, *Chem. Rev.*, 2003, **103**, 4883–4940.
54 H. Al-Abadleh, Aging of atmospheric aerosols and the role of iron in catalyzing brown carbon formation, *Environ. Sci.: Atmos.*, 2021, **1**, 297–345.
55 D. Kim, Y. Xiao, R. Karchere-Sun, E. Richmond, H. M. Ricker, A. Leonardi and J. G. Navea, Atmospheric Processing of Anthropogenic Combustion Particles: Effects of Acid Media and Solar Flux on the Iron Mobility from Fly Ash, *ACS Earth Space Chem.*, 2020, **4**, 750–761.
56 C. Szady, G. Picarillo, E. J. Davis, D. Drapanauskaite, K. Buneviciene, J. Baltrusaitis and J. G. Navea, Iron dissolution and speciation from combustion particles under environmentally relevant conditions, *Environ. Chem.*, 2023, **20**, 171–182.